A numerical characterization of the attractor for a fluid-structure interaction problem

Clara Patriarca, Filippo Calamelli, Paolo Schito, Tommaso Argentini and Daniele Rocchi

In this paper, starting from some known theoretical results, the long-term dynamics of a fluid-structure interaction problem for a Poiseuille flow through a 2D channel containing a rectangular obstacle are investigated from a numerical point of view. From a physical point of view, the wind-induced motions of the deck of a bridge are modeled similarly to a wind tunnel experiment at large times. In particular, we are concerned about the explicit characterization of the global attractor of the problem, that is the subset of the phase space to which eventually all the trajectories of the system approach.

1 Introduction

Nowadays, the understanding of the dynamic response to turbulent wind is a crucial issue in the design of long-span bridges. Numerous phenomena affect suspension bridges, like vortex-induced oscillations, buffeting and flutter instabilities (see [14, 17, 30]). Specifically, flutter instability occurs at high wind velocities ($> 70\ m/s$ for long-span bridges) at which the vertical and torsional motion of the deck synchronize, leading the deck to oscillate with growing amplitudes and eventually causing the bridge to collapse [2, 3, 15].

From an engineering point of view, the flutter instability onset can be predicted with different approaches, i.e. experimental, numerical or hybrid methods [11]. Experimental methods rely on wind tunnel testing of full-bridge aeroelastic models [5] while numerical approaches typically involve Computational Fluid Dynamics (CFD) simulations. Hybrid methods are widely employed due to the implementation complexity of aeroelastic models, and they usually combine numerical models of the structure with experimentally identified aerodynamic coefficients [4, 12, 13]. On the other hand, Scanlan's linearized theory constitutes the most widely used approach to estimate the flutter limit (see [26, 27, 30]). In the 2D case, a major contribution is

Keywords: fluid-structure problem, global attractor, numerical characterization
MSC 2020: Primary 74F10; secondary 35B41, 76M12

also due to Theodersen's inviscid flat-plate theory [32] and the approximate formula by Selberg [29]. These studies are used as a modeling framework to select which experimental coefficients are to be evaluated during wind tunnel tests, namely the so-called *flutter derivatives*.

From a mathematical point of view, aerodynamic instabilities can be studied by considering the asymptotic behavior of the body-fluid (bridge-wind) system as time goes to infinity. In general, any dynamical system, like the one at consideration, can be seen as described by the solution $y(t)$ of the differential equation:

$$\frac{dy(t)}{dt} = F_\lambda(y(t)), \tag{1.1}$$

where F is a mapping depending on some physical parameter λ. The phenomena that are observed depend on λ, which governs the transition of the system among different states. From an analytical point of view, it is not easy to predict to which state a given dynamical system will evolve as $t \to \infty$. However, to provide a proper description of the long-term dynamics, one usually searches small subsets of the phase space able to describe the typical behavior of the system, namely to attract all the orbits and reduce the degrees of freedom of the system. To this purpose, the most natural object to use in the theory of infinite-dimensional dynamical systems is the *global attractor* (see [9, 31]). For instance, in the context of fluid dynamics systems, the global attractor is the set confining all possible flows corresponding to all possible initial data. Once the existence of the global attractor is known, the spontaneous following question concerns the characteristics of such a set, which might be more or less complicated, even exhibiting a fractal nature.

Accordingly, the main purpose of this paper is to provide an explicit characterization of the global attractor associated with a fluid-structure interaction problem, by numerically modeling the deck of a suspension bridge interacting with wind, similarly to what is done in a wind tunnel experiment. Indeed, this could be considered comparable to the practical problem of determining which permanent state will be observed after a short transient period in a wind tunnel. To provide a description of the global attractor and, thus, create an explicit link between the analytical and experimental framework, we intervene through numerical simulations, by which we are able to capture some orbit of the dynamical system at consideration. In particular, we simulate the static and dynamic behavior of the cross-section of the deck immersed in a fluid flow at different conditions. Specifically, the deck is allowed to oscillate just in the vertical direction. The reason for this constraint is that the decoupling of the vertical and torsional degrees of freedom is a first step towards the assessment of the behavior of the deck of a bridge interacting with the wind.

Plan of the paper. The paper is organized as follows. In Section 2, we present a rigorous formulation of the model and we recall some analytical results about the well-posedness and long-term dynamics, in particular concerning the existence of the global attractor. In Section 3, the numerical strategy adopted is described. Section

4 reports the numerical results obtained in terms of the main objective of the paper and finally, in Section 5, some conclusions are drawn and the future developments are presented.

2 Problem formulation and analytical preliminaries

Our analysis is performed on a two-dimensional fluid-structure-interaction evolution problem inspired by the one introduced in [7], with some small exceptions that will be clearer as the model is described. We label as $B = [-d, d] \times [-\delta, \delta]$ a rectangular rigid body, with mass $m > 0$, representing the 2D (scaled) cross-section of the deck of a suspension bridge; we can assume d to be equal to 1, by using the length of the body as reference length scale. Such body is free to move vertically inside a 2D channel

$$\mathcal{R} = (-I, I) \times (-L, L),$$

driven by the action of both an elastic restoring force, the fluid flow and a viscous damping force describing the overall dissipation mechanism of the structure: see Figure 1.1. The upper and lower boundaries of the channel are denoted by $\Gamma = (-I, I) \times \{-L, L\}$, while h denotes the position of the barycentre of the rigid body from the middle line of the channel, $x_2 = 0$. Thus,

$$B_h = B + h\hat{e}_2 \quad \forall\, |h| < L - \delta$$

tracks the position of the body after the vertical translation. Notice that, when $|h| = L - \delta$, the obstacle collides with Γ. Due to the presence of the moving rigid body, the domain occupied by the fluid Ω_h depends itself on time through h, which explains the subscript, and it is given by:

$$\Omega_h = \mathcal{R} \setminus B_h \qquad \text{with} \qquad h = h(t).$$

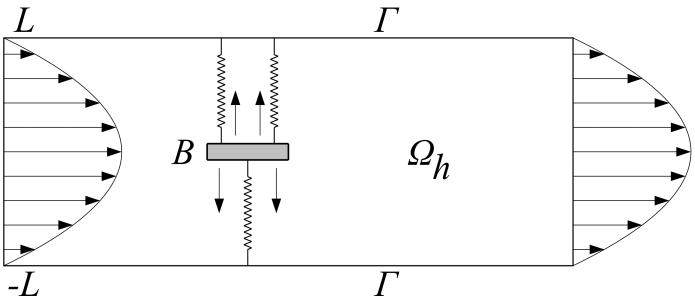


Figure 1.1. The channel with the vertically moving obstacle B

At the outlets of the channel, the velocity field reproduces a stationary Poiseuille flow profile, which we label as q_λ. Before formulating the problem, we emphasize that with an abuse of notation we use the Cartesian product

$$\Omega_{h(t)} \times (0,T)$$

to indicate the space-time domain given by $\{(x,t) \in \mathbb{R}^2 \times \mathbb{R} : 0 < t < T, x \in \Omega_h = \Omega_{h(t)}\}$. Let $\rho >$ be the density of the fluid. The problem can be then formulated as follows. Find (u,h) satisfying

$$\begin{gathered}
\rho\, u_t = \mu\, \Delta u - \rho\, (u \cdot \nabla) u - \nabla p, \quad \operatorname{div} u = 0 \qquad \text{in } \Omega_h \times (0,T), \\
u = q_\lambda(x_2) = \lambda(L^2 - x_2^2)\, \hat{e}_1 \quad \text{on } \partial\mathcal{R} \times (0,T), \qquad u = h'\, \hat{e}_2 \quad \text{on } \partial B_h \times (0,T), \\
m\, h'' + r h' + f(h) = -\hat{e}_2 \cdot \int_{\partial B_h} \mathcal{T}(u,p) \cdot \hat{n} \qquad \text{in } (0,T),
\end{gathered} \tag{2.1}$$

with the initial conditions $u(x,0) = u_0$, $h(0) = h_0$, $h'(0) = k_0$. In (2.1), the functions $u : \Omega_h \times (0,T) \to \mathbb{R}^2$ and $p : \Omega_h \times (0,T) \to \mathbb{R}$ are respectively the unknown velocity vector field and the unknown scalar pressure, whereas $\hat{n}$ is the outward normal to $\partial\Omega_h$, directed in the interior of ∂B_h. Given a prescribed pressure drop $G > 0$ and the kinematic viscosity of the fluid $\mu > 0$, the quantity $\lambda = G/(2\mu\rho)$ in q_λ measures the prescribed magnitude of the Poiseuille flow, thus λ is given. Notice that $U = \lambda\, L^2$ corresponds to the maximum velocity at the inlet and outlet. The ODE in (2.1) governs the motion of the body: $f(h)$ is an elastic smooth nonlinear restoring force (linear for small displacements), $r\, h'$ is the viscous damping force with a damping coefficient $r > 0$, and $\mathcal{T}(u,p) = -p\mathbf{I} + 2\mu D(u)$ is the fluid Cauchy stress tensor, with $\mathbf{I}$ the 2×2-identity matrix and

$$D(u) = \frac{1}{2}(\nabla u + \nabla u^T).$$

In other words, the right-hand side of the ODE in (2.1) corresponds to the fluid lift. Some further hypotheses on $f(h)$ will be given in the following paragraph.

The steady problem associated with (2.1) reads as follows. Find (u_s, h_s) satisfying

$$\begin{gathered}
-\mu\, \Delta u_s + \rho (u_s \cdot \nabla) u_s + \nabla p_s = 0, \quad \operatorname{div} u_s = 0 \qquad \text{in } \Omega_{h_s}, \\
u_s = q_\lambda \quad \text{on } \partial\mathcal{R}, \qquad u_s = 0 \quad \text{on } \partial B_{h_s},
\end{gathered} \tag{2.2}$$

together with the static fluid-structure-interaction condition

$$f(h_s) = -\hat{e}_2 \cdot \int_{\partial B_{h_s}} \mathcal{T}(u_s, p_s) \cdot \hat{n}. \tag{2.3}$$

In the following paragraphs, we provide some analytical preliminaries necessary to develop our analysis.

Well-posedness of the model. We now present an overview of the well-posedness results both for problem (2.1) and (2.2)-(2.3). To this purpose, we describe the functional setting for our problem. For every $h \in (-L+\delta, L-\delta)$, we denote by $W^{m,q}(\Omega_h)$, $m \geq 0$, $q \geq 1$, the usual Sobolev space of functions on Ω_h having all derivatives up to order m summable to the q-th power; also $W^{0,q}(\Omega_h) = L^q(\Omega_h)$. The norm associated to the space is denoted by $\|\cdot\|_{W^{m,q}(\Omega_h)}$ and $\|\cdot\|_{W^{0,q}(\Omega_h)} = \|\cdot\|_{L^q(\Omega_h)}$. Given $h = h(t)$ a function from $[0,T]$ to $(-L+\delta, L-\delta)$, we define the following spaces:

$$L^p(0,T;W^{1,2}(\Omega_{h(t)})) = \Big\{ f : [0,T] \to W^{1,2}(\Omega_{h(t)}) \quad \text{s.t.} \\ \|f\|^p_{L^p(0,T;W^{1,2}(\Omega_{h(t)}))} = \int_0^T \|f(t)\|^p_{W^{1,2}(\Omega_{h(t)})}\, dt < +\infty \Big\}$$

for $1 \leq p < \infty$, and

$$L^\infty(0,T;L^2(\Omega_{h(t)})) = \Big\{ f : [0,T] \to L^2(\Omega_{h(t)}) \quad \text{s.t.} \\ \|f\|_{L^\infty(0,T;L^2(\Omega_{h(t)}))} = \operatorname*{ess\,sup}_{t\in[0,T]} \|f(t)\|_{L^2(\Omega_{h(t)})} < +\infty \Big\}.$$

The well-posedness results are given by assuming some further assumptions on the elastic force f. In particular

$$f \in C^1(-L+\delta, L-\delta) \quad \text{satisfies} \quad f(0) = 0 \quad \text{and} \quad f'(h) > 0 \quad \forall\, h \in (-L+\delta, L-\delta). \tag{2.4}$$

Moreover, we require f to be a *strong force*, that is

$$\exists\, r > 0 \qquad \text{s.t.} \qquad \lim_{|h|\to L-\delta} |f(h)| \exp\left\{ -\frac{1}{(L-\delta-|h|)^{4+r}} \right\} = +\infty. \tag{2.5}$$

In the following theorem, we provide a well-posedness result for the steady problem (2.2)-(2.3). Solutions to (2.2)-(2.3) represent equilibrium positions of the body, for a given flow regime of the fluid.

Theorem 2.1. *Assume that f satisfies* (2.4)-(2.5). *For any $\lambda > 0$ the problem* (2.2)-(2.3) *admits a weak solution. Furthermore, there exists $\lambda_s > 0$ such that if $\lambda < \lambda_s$ the problem* (2.2)-(2.3) *admits a unique weak solution $(u_s, h_s) \in W^{1,2}(\Omega_{h_s}) \times (-L+\delta, L-\delta)$ given by $(u_\lambda, 0)$, that is u_s, with $h_s = 0$. Moreover, there exists $C(\lambda) > 0$, with $C(\lambda) \to 0$ as $\lambda \to 0$, such that*

$$\|\nabla u_\lambda\|_{L^2(\Omega_0)} \leq C(\lambda).$$

For the proof, we refer to [7] and to [18, Theorem 2.2] for the adaptation to the case of a channel with finite length. Theorem 2.1 provides an intuitive result as it guarantees that the equilibrium position is unique and symmetric when the Poiseuille

flow rate is sufficiently small. Moving to the evolution problem (2.1), from [24] (see also [18]) we infer a well-posedness result. Before stating it, we just emphasize that the presence of a viscous damping force rh' in the ODE in (2.1) does not change any of the results that we are about to show in the remaining part of the section. Then

Theorem 2.2. *Assume that f satisfies* (2.4)-(2.5). *Moreover let $|h_0| < L - \delta$ and u_0 be such that $u_0 \cdot \hat{n} = k_0 \hat{e}_2 \cdot \hat{n}$ on ∂B_{h_0}. Then, problem* (2.1) *admits a unique weak solution (u, h) such that*

$$(u, h) \in [L^2(0, T; W^{1,2}(\mathcal{R})) \cap L^\infty(0, T; L^2(\mathcal{R}))] \times W^{1,\infty}(0, T; (-L + \delta, L - \delta))$$

and $u|_{B_h} = h' \hat{e}_2$, for any $T < \infty$. Moreover the energy of (u, h) is bounded.

We conclude this paragraph with a remark about assumption (2.5).

Remark 2.3. The elastic force $f(h)$ prevents the obstacle from going excessively far from the equilibrium position due to the strong force assumption (2.5). This reinforces the physical representativeness of the model since the areodynamic and aeroelastic response is not expected to be accurately described, from the numerical point of view, when the obstacle is close to the boundary of the channel.

Long-time behavior. We here present the long-time characteristics of the dynamical system associated with problem (2.1). First, we state the convergence of the solutions of (2.1) to the unique steady state, if λ is sufficiently small. In other words, we guarantee that the equilibrium solution is stable.

Theorem 2.4. *Let $R > 0$ be arbitrarily fixed and λ_s as in Theorem* 2.1. *There exists $\lambda_1 = \lambda_1(R) \in (0, \lambda_s)$ such that if $\lambda < \lambda_1$, the weak solution (u, h) of problem* (2.1)*, with initial position of the obstacle $h_0 = 0$ and initial velocities $z_0 = (u_0, k_0) \in L^2(\Omega_0) \times \mathbb{R}$ such that $\|u_0\|_{L^2(\Omega_0)} + m{k_0}^2 \leq R^2$, converges to the solution $(u_\lambda, 0)$ of* (2.2)-(2.3) *in $L^2(\Omega_0)$ as $t \to \infty$.*

For the proof, we refer to [18, Theorem 4.1]. From the well-posedness of problem (2.1) given by Theorem 2.2, we obtain that there exists a map, which we refer to as *semiflow*, yielding from all initial data the solution at any positive time t. This map is uniquely determined by the problem; with reference to (1.1), this map corresponds to F, depending on the parameter λ measuring the magnitude of the Poiseuille flow, while $y = (u, h)$ is the unique solution to (2.1). For a detailed description of the semiflow map, we suggest to the reader the paper [18] and the relative references. In this context, it suffices to know that the determination of such map allows investigatung the existence of the global attractor, that is, as already mentioned, the most effective tool in the theory of infinite-dimensional dynamical system to describe the long-term dynamics. Indeed, the global attractor is a compact subset of the phase space to which all the solutions (u, h) to problem (2.1) eventually approach. The following theorem, proven in [18], provides the existence of this set.

Theorem 2.5. *Problem* (2.1) *generates a semiflow that possesses the global attractor.*

Theorem 2.5 deserves few comments, as it is the starting point for the main analysis of the paper. Although it guarantees the substantial reduction of the degrees of freedom of the system, Theorem 2.5 is formulated in an abstract sense and it does not give any explicit characterization of the attractor. However, combining this result together with Theorem 2.4, we obtain a first explicit characterization of the attractor in a particular situation: if the Poiseuille flow rate is sufficiently small, the attractor reduces to the unique equilibrium solution of problem (2.1). Our objective is precisely to cover other situations through a numerical simulation process, in order to provide an explicit description of the global attractor for any range of the incoming flow.

3 Simulation strategy

In this section, the numerical settings and schemes adopted for the simulations are described. The analyses were performed in two stages, labeled as *static* and *dynamic* cases. During the static stage, a Poiseuille flow impinges the fixed obstacle at different flow rates. The static case was used both as a starting point to validate the chosen numerical setting and to obtain a description of the flow field at different values of the inlet velocity magnitude. As for the dynamic stage, the deck cross-section interacts with the fluid through a vertical translation. Specifically, the global attractor associated with the dynamical system is characterized by describing the behavior of the velocity field of the fluid and the position of the obstacle in the long term.

Following the numerical strategy presented in [10], the simulations were carried out considering an aspect ratio for the obstacle d/δ equal to 5. As shown in Figure 1.2, the computational domain was characterized by an along wind length and a height respectively equal to $30\,d$ and $14.2\,d$. Moreover, the windward edge of the obstacle was located at a distance $8\,d$ from the inlet.

The same mesh was adopted for both the static and the dynamic case. Specifically, the fluid domain was divided into seven regions with different refinements. Close to the boundaries of the obstacle, the mesh size is $2.7 \times 10^{-3}\,d$, resulting in a dimensionless wall distance $y^+ < 5$ almost everywhere, and it is coarsened up to a maximum of $0.35\,d$ in the wake. Overall, the mesh consists of 50000 cells, see Figure 1.2.

A RANS-based modeling technique was employed, adopting the well-known ($k-\omega$ SST) turbulence model. This closure model is one of the most commonly exploited in the context of RANS simulations [10] since it exhibits a more reliable behavior when predicting separating flows with respect to other turbulence models. Second-order schemes were selected for all quantities both in space and time and a PISO scheme was used for the velocity-pressure coupling. At the inlet of the computational domain, a parabolic velocity profile was imposed and Dirichlet boundary conditions were set for both the turbulence kinetic energy k and the specific dissipation rate ω. Moreover, Neumann boundary conditions were imposed for the pressure. The inlet turbulence intensity was set equal to 1% with a value of the turbulence viscosity ratio $\nu/\nu_t = 2$, where ν_t is the turbulence kinematic viscosity. It is worth pointing out that the $k-\omega$

SST turbulence model is quite stable with respect to the inlet boundaries [10] and thus, with this approach, it is not possible to faithfully reproduce the experimental wind tunnel inlet conditions. A no-slip condition was imposed on the top and bottom sides of the domain, to keep the parabolic profile unchanged up to the windward edge of the obstacle. Finally, wall functions were employed for the near-wall treatment of the obstacle. The time step was chosen so as to guarantee a value of the Courant number lower than 1 almost everywhere, with a maximum of approximately 2 in very small areas around the corners. The simulations were performed with the open-source software OpenFOAM [1]. The next paragraphs treat the specific settings for the static and dynamic simulations.

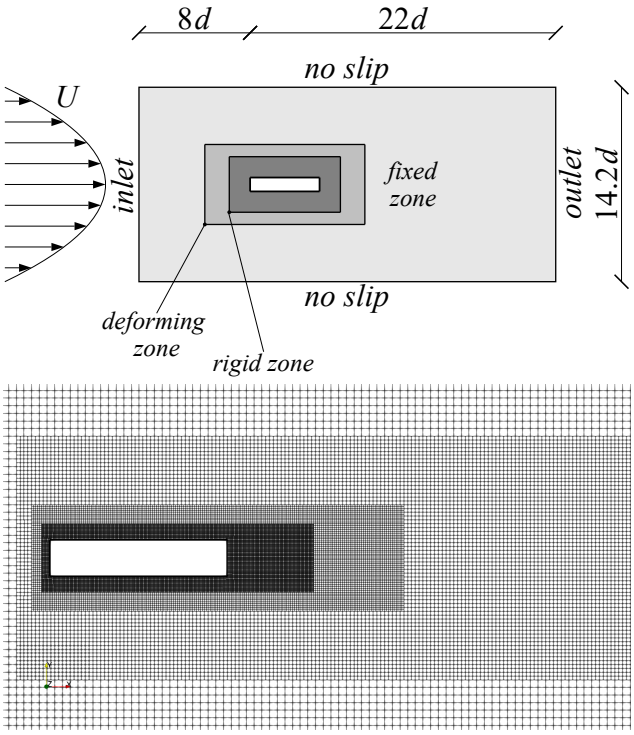


Figure 1.2. The figure above depicts a sketch of the computational domain while the figure below reports a close up of the mesh structure adopted near the obstacle.

3.1 Static case

Let U be the maximum velocity of the parabolic profile at the inlet. We define the Reynolds number as

$$Re = \frac{U\delta}{\nu},$$

and thus, given that $U = \lambda L^2$, we consider the variations of Re rather than the variations of λ. Another meaningful dimensionless parameter is the so-called Strouhal number, defined as

$$St = \frac{f_w \delta}{U},$$

where f_w is the vortex shedding frequency, as well as the Scruton number

$$Sc = \frac{2\pi m \xi}{\rho \delta^2},$$

where m and ξ are respectively the linear mass and the damping ratio of the system while ρ is the density of the fluid. Let the dimensionless time t^* be defined as

$$t^* = \frac{t\,U}{\delta}.$$

Figure 1.4 shows the time histories, obtained through the simulations, of the dimensionless drag C_D, lift C_L and moment C_M for $U = 1$, corresponding to $Re \approx 1.3 \times 10^4$. As expected, the lift coefficient oscillates around zero. Indeed, it is well-known both from a theoretical and an experimental point of view (see [19, 20, 23]) that no lift is exerted on a bluff body immersed in a viscous fluid whenever its cross-section is symmetric with respect to the angle of attack. Table 1.1 compares the time-averaged values of the aerodynamic coefficients and the Strouhal number with the experimental ones taken from the literature [28]. It is worth pointing out that, in this specific context, if the Reynolds number is not sufficiently large, the values of the moment are not available, see [28, Section 3]. Figure 1.3 depicts the comparison between the numerical values of the Strouhal number, as a function of Re, and the experimental data taken from [28]. A reasonable agreement between the numerical and the experimental results allows validating the chosen setting.

	CL	CD	CM	St
Experimental	0.08 (rms)	1.03	——	0.11
Numerical	-0.0013	1.004	-1.519×10^{-4}	0.118

Table 1.1. Comparison between the numerical and experimental time-averaged aerodynamic coefficients (experimental data taken from [28]).

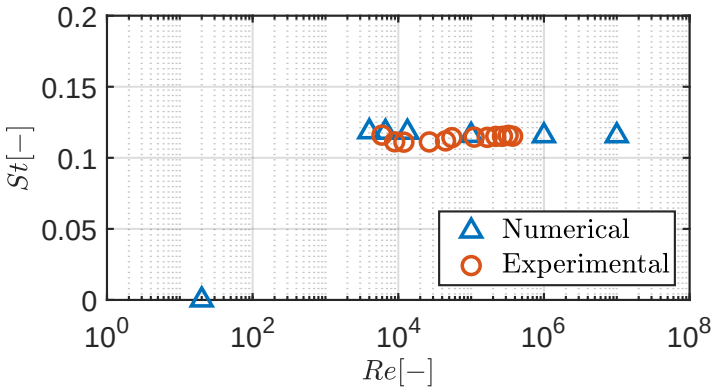


Figure 1.3. Numerical and experimental [28] Strouhal number as a function of Re.

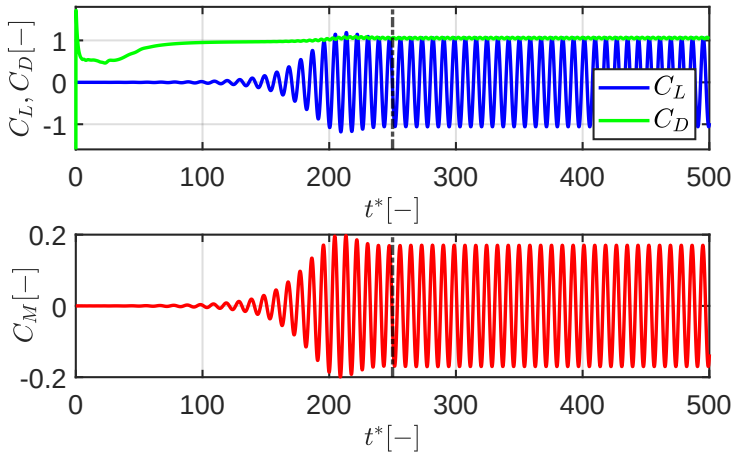


Figure 1.4. Time traces of the numerical lift, drag and moment. The figures report just a portion of the time histories. The dotted black line indicates the end of the transient stage.

3.2 Dynamic case

As previously mentioned, in the dynamic case the obstacle is allowed to move in the vertical direction. Following the literature [8, 10, 22, 25], the mesh is organized in three regions (see Figure 1.2): a boundary layer rigid motion region, a deforming region and a non-deforming region. The first is defined close to the rigid body profile so that all the mesh nodes identically move through a rigid translation. The mesh in the deforming region is modified by the body motion at each time step while the non-deforming zone is fixed.

Before discussing the results, we conclude with a remark on the relation between the model considered to obtain the analytical result in Section 2 and the model adopted for the computational analyses.

Remark 3.1. The numerical model differs from the analytical one presented in Section 2 in one aspect. Specifically, in the numerical model the obstacle is subjected to a linear elastic force while, in the analytical one, $f(h)$ satisfies conditions (2.5). The introduction of the restoring force $f(h)$ satisfying (2.5) in problem (2.1) comes from the necessity to avoid collisions, by which one is able to prove Theorems 2.1, 2.2 and Theorem 2.5. A posteriori, we observed that, in the numerical framework, collisions are prevented by the computational setting itself and thus, it makes sense to substitute $f(h)$ with its first order approximation $f(h) \sim -kh$, where $k > 0$. All the analytical results presented in Section 2 still hold for the numerical problem.

4 Results and discussion

In this section, the numerical results are presented, giving a general discussion and an explicit characterization of the global attractor associated with the fluid-structure interaction system.

As for the static simulation, a qualitative description of the flow topology varying Re is depicted in Figures 1.5, 1.6 and 1.7. The instantaneous flow fields and streamlines all correspond to the non-dimensional time $t^* = t^*_{regime} + 500$, where t^*_{regime} has been identified through the time history of the aerodynamic coefficients. For $Re = 30$, the streamlines are characterized by an upstream-downstream symmetry. In particular, it is possible to observe the presence of two symmetrical eddies in a closed re-circulation zone in the wake of the obstacle and, thus, the flow can be considered steady.

A different regime is observed at $Re \approx 1.3 \times 10^4$, see Figures 1.5 and 1.7. The flow becomes unsteady and time-periodic, and we can observe the appearance of the Von Kármán wake, typically characterizing the vortex shedding phenomenon. From a mathematical point of view, this implies the occurrence of a so-called *Hopf* unsteady bifurcation, see [16] for a rigorous description of the phenomenon. The same regime is observed also for $Re = 10^5, 10^6, 10^7$, see Figure 1.6 and 1.7. In all cases, the vortexes shed from the obstacle with a specific frequency. This phenomenon can be also interpreted in the light of Figure 1.3. Specifically, at sufficiently high Re, the Strouhal number is non-zero, suggesting the presence of time-periodic flow mechanisms. The fact that the flow never becomes unstable, even when considering very high Re, is probably due to the usage of a RANS-based model. Indeed, it is well-known from the state-of-the-art [10] that RANS approaches, although being computationally convenient, mostly lose capturing the unstable features of the flow. RANS-based models assume a stationary turbulent regime, which prevents from sizing highly irregular velocity fluctuations. As a consequence, although capturing the average

changes in topology, we do not observe the generation of a turbulent wake as observed in [6, 21].

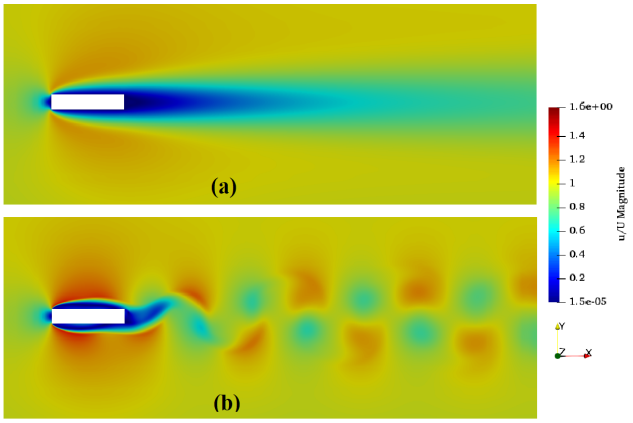


Figure 1.5. Instantaneous flow field at $t^* = t_{regime} + 500$ for different Reynolds number (a) $Re = 30$; (b) $Re \approx 1.3 \times 10^4$.

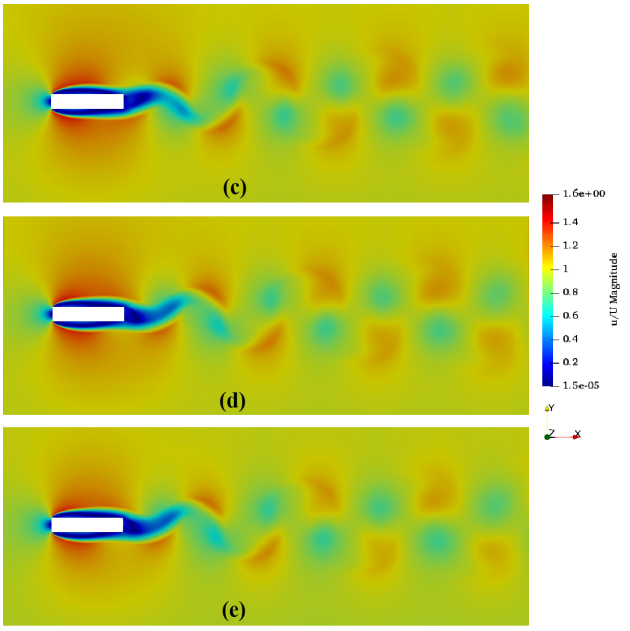


Figure 1.6. Instantaneous flow field at $t^* = t_{regime} + 500$ for different Reynolds number (c) $Re = 10^5$; (d) $Re = 10^6$; (e) $Re = 10^7$.

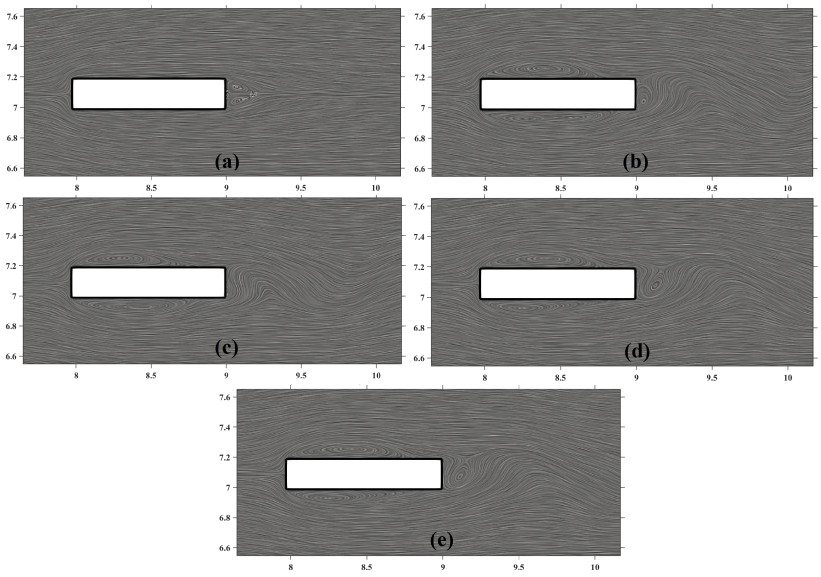


Figure 1.7. Instantaneous streamlines obtained with the LIC technique at $t^* = t_{regime} + 500$ for different Reynolds number (a) $Re = 30$; (b) $Re \approx 1.3 \times 10^4$; (c) $Re = 10^5$; (d) $Re = 10^6$; (e) $Re = 10^7$.

Regarding the dynamic case, as observed in the static simulations, increasing Re the flow pattern makes a transition from a fully symmetrical and steady configuration to an unsteady periodical one, where it exhibits a vortex shedding phenomenon. This naturally influences the dynamics of the body, leading to vortex-induced vibrations whose one of the most relevant features is the so-called *lock-in* effect. Figure 1.8 depicts a time history of the dimensionless vertical displacement, obtained imposing a maximum inlet velocity equal to $1.15m/s$, which leads to a Re approximately equal to 10^4. In particular, we observe that the obstacle oscillates around the equilibrium position $h_{eq} = 0$.

As soon as the vortex shedding frequency becomes equal to the natural frequency of the structure, a resonance phenomenon occurs and the body may be subjected to large amplitude oscillations. If f_n is the natural frequency of the body, for the 1-DOF system at consideration, the onset of resonance occurs when

$$U = U_{St} = \frac{f_n \delta}{St}.$$

Defining the reduced velocity $U^* = \frac{U}{f_n \delta}$, the vortex shedding synchronizes with the natural frequency of the structure at $U^* = \frac{1}{St}$. Subsequently, the motion of the obstacle starts contributing to the coherence of the flow eddies, capturing the shedding frequency by locking it to the natural frequency of the structure and spreading the lock-in effect on a range of velocities around U_{St}.

In Figure 1.9(a), it is reported the maximum non-dimensional amplitude of oscillation at regime as a function of the reduced velocity ($h_{eq} = 0$ is the position of the body given by the unique stationary solution, see Theorem 2.1). Figure 1.9(b) shows the non-dimensional vortex shedding frequency versus the reduced velocity. Both plots are built considering two regimes for the Reynolds number Re and increasing the stiffness of the system accordingly. It is possible to observe the synchronization between the vortex shedding and the natural frequency of the system for a specific range of reduced velocities around the predicted value $U^* = 1/St$, inducing the body to reach its maximum vibration amplitude. Furthermore, increasing the stiffness of the system, the Scruton number Sc decreases from 256.4 to 7.0 and, as expected, the maximum non-dimensional amplitude of oscillation increases.

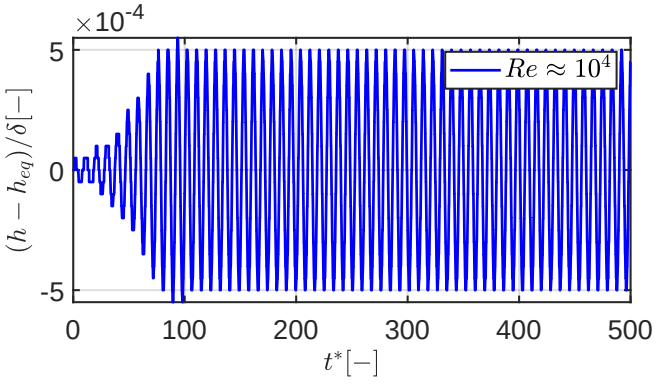


Figure 1.8. Time history of the structural motion for $Re \approx 10^4$.

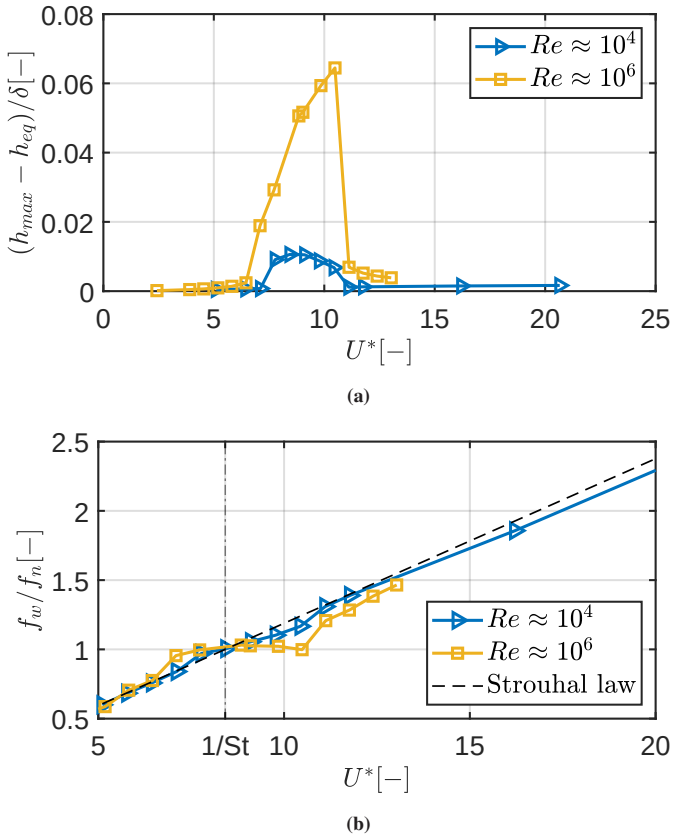


Figure 1.9. Figure (a): non-dimensional amplitudes of oscillation of body versus the reduced velocity U^*. Figure (b): vortex shedding frequency over the natural frequency of the system as a function of the reduced velocity U^*.

In the last paragraph of this section, a reinterpretation of the previous results is given in terms of the main purpose of the article, i.e. giving an explicit characterization of the global attractor associated with the dynamical fluid-structure system. In view of the numerical observations that we have described, we can identify two (three) different regimes (subregimes) as a function of λ:

(i) If λ is sufficiently small, specifically lower than a critical value $\lambda < \lambda_c$, the attractor reduces to a one-point set in the phase space, corresponding to the unique symmetrical stationary solution $(u_s, h_s) = (u_\lambda, 0)$ given by Theorem 2.1 and thus, the dimension of the attractor is 0. The flow topology corresponding to this solution is reported in Figures 1.5(a) and 1.7(a). This is in accordance with the result already proven in Theorem 2.4 and thus, $\lambda_c = \lambda_1$.

(ii) As soon as $\lambda > \lambda_c$, a Hopf bifurcation occurs and, after a short transient motion, the dynamics of the problem becomes time-periodic. In other words, given $y(\cdot) = (u(\cdot), h(\cdot))$ the unique solution to (2.1), we have that $y(\cdot)$ converges to a non-symmetrical time-periodic solution $\varphi(\cdot)$ to problem (2.1). The global attractor reduces in this case to the orbit of $\varphi(\cdot)$ and therefore, it corresponds to a closed curve. However, we can identify two subregimes, $\lambda_c < \lambda_{c_1} < \lambda < \lambda_{c_2}$ and $\lambda_c < \lambda < \lambda_{c_1} \vee \lambda_{c_2} < \lambda$, where the time-periodic solution to which $y(\cdot)$ converges drastically changes, at least from a quantitative point of view. Indeed, according to the value of λ, we are inside or outside what we have previously described as the lock-in range. As shown in Figure 1.9, the structure motion inside the lock-in range may reach large amplitudes of vibration. As a result, although the global attractor still corresponds to the orbit of a time-periodic solution, i.e. to a closed curve, this orbit might deform consistently to the value of λ. The threshold values λ_{c_1} and λ_{c_2} can be defined numerically, as it was done in Figure 1.9 for two Re regimes.

In principle, we might expect that the structure of the global attractor further complicates as λ increases. Specifically, this would correspond to a chaotic structure for the flow, exhibiting random variations of velocity and pressure in time and space. However, as already mentioned, due to the numerical methods adopted, we are able to catch only the average stable features of the flow.

5 Conclusions and further developments

Starting from some known theoretical results, numerical simulations of the flow past a rectangular obstacle were presented. Specifically, two different simulation strategies were adopted: the static one considers the obstacle fixed while the dynamic case allows its vertical translation. In order to give an explicit characterization of the global attractor associated with the problem, different Re regimes were investigated, capturing significant variations of the system dynamics. In particular, when the vortex shedding and the natural frequency of the motion of the obstacle synchronize, it is possible to note a remarkable increase in the amplitudes of vibration, which could be identified as a lock-in effect.

As for the future steps, the most natural developments of the work would be to perform Large Eddies Simulations (LES) of the problem, as well as including the torsional degree of freedom in the motion of the obstacle. Specifically, LES are computationally more expensive with respect to RANS simulations but, on the other hand, they would allow to capture some turbulent features of the flow and thus, improve the characterization of the structure of the global attractor.

Bibliography

[1] OpenCFD. *OpenFOAM Programmer's Guide, Springer* (2004)

[2] T. Agar, The analysis of aerodynamic flutter of suspension bridges. *Computers & Structures* **30**, 593–600 (1988)

[3] T. Agar, Aerodynamic flutter analysis of suspension bridges by a modal technique. *Engineering Structures* **11**, 75–82 (1989)

[4] T. Argentini, G. Diana, D. Rocchi and C. Somaschini, A case-study of double multi-modal bridge flutter: Experimental result and numerical analysis. *Journal of Wind Engineering and Industrial Aerodynamics* **151**, 25–36 (2016)

[5] T. Argentini, D. Rocchi and C. Somaschini, Effect of the low-frequency turbulence on the aeroelastic response of a long-span bridge in wind tunnel. *Journal of Wind Engineering and Industrial Aerodynamics* **197**, 104072 (2020)

[6] S. Berrone, V. Garbero and M. Marro, Numerical simulation of low-reynolds number flows past rectangular cylinders based on adaptive finite element and finite volume methods. *Computers and Fluids* (2011)

[7] D. Bonheure, G. Galdi and F. Gazzola, Equilibrium configuration of a rectangular obstacle immersed in a channel flow. *Comptes Rendus. Mathématique* **358**, 887–896 (2020)

[8] F. Brusiani, S. de Miranda, L. Patruno, F. Ubertini and P. Vaona, On the evaluation of bridge deck flutter derivatives using rans turbulence models. *J. Wind Eng. Ind. Aerodyn.* **119**, 39–47 (2013)

[9] V. Chepyzhov and M.I.. Vishik, *Attractors for equations of mathematical physics*. American Mathematical Society Colloquium Publications, 49. American Mathematical Society, Providence, RI, 2002. (2002)

[10] S. De Miranda, L. Patruno, F. Ubertini and G. Vairo, On the identification of flutter derivatives of bridge decks via rans turbulence models: Benchmarking on rectangular prisms. *Engineering Structures* **76**, 359–370 (2014)

[11] G. Diana, D. Rocchi and M. Belloli, Wind tunnel: a fundamental tool for long-span bridge design. *Structure and Infrastructure Engineering* **11**, 533–555 (2015)

[12] G. Diana, S. Stoyanoff, K. Aas-Jakobsen, A. Allsop, M. Andersen, T. Argentini, M. C. Montoya, S. Hernández, J. Ángel Jurado, H. Katsuchi, I. Kavrakov, H.-K. Kim, G. Larose, A. Larsen, G. Morgenthal, O. Øiseth, S. Omarini, D. Rocchi, M. Svendsen and T. Wu, Iabse task group 3.1 benchmark results. part 2: Numerical analysis of a three-degree-of-freedom bridge deck section based on experimental aerodynamics. *Structural Engineering International* **30**, 411–420 (2020)

[13] G. Diana, S. Stoyanoff, K. A.-J. Dr, A. Allsop, M. Andersen, T. Argentini, M. C. Montoya, S. Hernández, J. Ángel Jurado, H. Katsuchi, I. Kavrakov, H.-K. Kim, G. Larose, A. Larsen, G. Morgenthal, O. Øiseth, S. Omarini, D. Rocchi, M. Svendsen and T. Wu, Iabse task group 3.1 benchmark results. part 1: Numerical analysis of a two-degree-of-freedom bridge deck section based on analytical aerodynamics. *Structural Engineering International* **30**, 401–410 (2020)

[14] E. Dowell, *A Modern Course in Aeroelasticity, 5th ed.* Springer (2015)

[15] J. Frandsen, Numerical bridge deck studies using finite elements. part i: flutter. *Journal of Fluids and Structures* **19**, 171–191 (2004)

[16] G. Galdi, *Navier–Stokes equations: A Mathematical Analysis*. Springer New York (2009)

[17] F. Gazzola, *Mathematical Models for Suspension Bridges - Nonlinear Structural Instability*. Springer-Verlag (2015)

[18] F. Gazzola, V. Pata and C. Patriarca, Attractors for a fluid-structure interaction problem with time-dependent phase space, preprint (2021)

[19] F. Gazzola and C. Patriarca, An explicit threshold for the appearance of lift on the deck of a bridge. *J. Math. Fluid Mech.* **24, no. 1, Paper No. 9** (2022)

[20] F. Gazzola and G. Sperone, Steady Navier-Stokes equations in planar domains with obstacle and explicit bounds for its unique solvability. *Arch. Ration. Mech. Anal.* **238**, 1283–1347 (2020)

[21] K. Hourigan, M. Thompson and B. Tan, Self-sustained oscillations in flows around long blunt plates. *Journal of Fluids and Structures* **15**, 387–398 (2001)

[22] L. Huang, H. Liao, B. Wang and Y. Li, Numerical simulation for aerodynamic derivatives of bridge deck. *Simulation Modelling Practice and Theory* 719–729 (2009)

[23] M.P. Païdoussis, S.J. Price and E. De Langre, *Attractors of Evolutions Equations*. Cambridge University Press (2011)

[24] C. Patriarca, Existence and uniqueness result for a fluid-structure-interaction evolution problem in an unbounded 2D channel. *To appear in Nonlinear Differential Equations and Applications NoDEA* (2022)

[25] L. Patruno, Accuracy of numerically evaluated flutter derivatives of bridge deck sections using rans: Effects on the flutter onset velocity. *Engineering Structures* 49–65 (2015)

[26] R. Scanlan, The action of flexible bridges under wind, I: flutter theory. *Journal of Sound and Vibration* **60** (1978)

[27] R. Scanlan and J. Tomko, Airfoil and bridge deck flutter derivatives. *ASCE Journal of Engineering Mechanics Division* 1717–1737 (1971)

[28] G. Schewe, Reynolds-number-effects in flow around a rectangular cylinder with aspect ratio 1:5. *Journal of Fluids and Structures* 15–26 (2013)

[29] A. Selberg, Oscillation and aerodynamic stability of suspension bridges. *Technical Report Acta Polytechnica, Scandinavica Cil3* (1961)

[30] E. Simiu and R. Scanlan, *Wind Effects on Structure*. Wiley-Interscience Publication (1966)

[31] R. Temam, *Infinite-Dimensional Systems in Mechanics and Physics*. Springer (1997)

[32] T. Theodorsen, General theory of aerodynamic instability and the mechanism of flutter. *Technical Report 496, NACA* (1935)

Clara Patriarca
Department of Mathematics, Politecnico di Milano
clara.patriarca@polimi.it

Filippo Calamelli
Department of Mechanical Engineering, Politecnico di Milano
filippo.calamelli@polimi.it

Paolo Schito
Department of Mechanical Engineering, Politecnico di Milano
paolo.schito@polimi.it

Tommaso Argentini
Department of Mechanical Engineering, Politecnico di Milano
tommaso.argentini@polimi.it

Daniele Rocchi
Department of Mechanical Engineering, Politecnico di Milano
daniele.rocchi@polimi.it